Available online at www.sciencedirect.com

jmr&t Journal of Materials Research and Technology

journal homepage: www.elsevier.com/locate/jmrt

Original Article

Controlling the phase transformation window during stages of hot/cold forging of Ni-rich Ni–Ti alloy

Patrícia Freitas Rodrigues [a,*], *Hatim Reshie* [b], *Talita Gama de Sousa* [c], *Andersan dos Santos Paula* [c], *Francisco Manuel Braz Fernandes* [d], *Ritwik Basu* [e]

[a] *Univ Coimbra, CEMMPRE, Department of Mechanical Engineering, 3030-788, Coimbra, Portugal*
[b] *Department of Mechanical and Manufacturing Engineering, Manipal Institute of Technology, Manipal Academy of Higher Education (MAHE), Manipal, 576104, Karnataka, India*
[c] *Materials Engineering Section-SE-8, Instituto Militar de Engenharia – IME, Rio de Janeiro, RJ, Brazil*
[d] *CENIMAT, Department of Materials Science, FCT/UNL, 2829-516, Caparica, Portugal*
[e] *Kalyani Center for Technology & Innovation (KCTI), Bharat Forge Limited, Survey No. 15, Keshav Nagar, Pune, 411 036, MH, India*

ARTICLE INFO

Article history:
Received 30 June 2021
Accepted 3 October 2021
Available online 8 October 2021

Keywords:
Synchrotron radiation X-ray diffraction
Electron back-scattered diffraction
Shape memory alloys
Thermomechanical process

ABSTRACT

A detailed microstructural analysis during the intermediate stages of fabrication of NiTi orthodontic archwire is carried out in this study. These microstructural findings were related to the phase transformation characteristics such as start and finish transformation temperature, thermal hysteresis, etc. The objective was to monitor the transformation window during the different stages of thermomechanical processing. The casted alloy was further subjected to combinations of hot and cold forging steps with intermediate annealing. Four different sample conditions were prepared. The microstructure development in these samples was studied through electron back-scattered diffraction and synchrotron radiation X-ray diffraction (SR-XRD) techniques. The phase transformation temperatures were determined by differential scanning calorimetric measurements. The microstructures showed grain boundary serrations, very large grains of austenite, twin-like features within austenite grains and mixed-phase distribution of austenite and martensite. The differences in microstructures were also clear in terms of local in-grain misorientation and grain boundary fractions. SR-XRD measurements further revealed possible precipitation of Ni_4Ti_3 and Ni_3Ti. The martensite start temperature (M_s) was seen to be a clear function of high angle grain boundary fraction, while the finish temperature (M_f) showed an inverse trend. The transformation interval, M_s–M_f is related to the stored energy of austenite grains that determines the driving force to overcome the frictional work opposing the movement of the habit plane, while and A_f –A_s largely depends on the elastic

* Corresponding author.
E-mail address: pf.rodrigues@uc.pt (P. Freitas Rodrigues).
https://doi.org/10.1016/j.jmrt.2021.10.008

energy stored of the martensite plates during its growth. The hysteresis during reverse transformation (M → A) was related to the local in-grain misorientation.

1. Introduction

Ni–Ti based alloys are of interest on account of their unique properties, the shape memory effect (SME) and superelasticity (SE), making them attractive candidates for applications such as aerospace [1–3], biomedical engineering [4–6], and robotics [7,8] to list a few. Both these effects are the result of a reversible solid–solid phase transformation, high-temperature, high-symmetry phase B2 (austenite) ↔ low symmetry phase B19′ (martensite) either through thermal or stress inducement [9,10]. The latter decides superelasticity. This readily relates to thermoelastic transformation with twinning as the mode of deformation or self-accommodation.

Since superelastic behavior in these alloys is observed under isothermal conditions, applications requiring a well-controlled temperature environment are most effective, e.g., in the human body. Use of superelastic Ni–Ti alloys is discussed in a wide range of biomedical applications, which include dental surgeries and implants [11,12], endoscopy and cardiovascular treatments [12,13]. The majority of these superelastic Ni–Ti biomedical devices are fabricated from wires. Having these materials in the form of wire, the inherent disadvantage of slow response due to limitation on the cooling rate can be significantly overcome because of the high surface/volume ratio [14]. Extensive use of this material is found in orthodontic arch-wires. These archwires display a low modulus of elasticity in combination with a high strength that allows to bear large elastic deformation due to the 'spring-back' nature [15]. The superelastic response in these wires can be governed by specific thermodynamic relations that act as a driving force for the transformation. A correlation exists between the thermal hysteresis and the superelastic strain. The larger the hysteresis, the higher is the recoverable strain seen in shape memory effect. This leads to a higher superelastic strain of the binary alloy [16]. Furthermore, the plateau stress in a superelastic cycle can be related to the change in enthalpy through Clausius–Clapeyron equation [17]:

$$\frac{d\sigma}{dT} = \frac{-\Delta H}{T\varepsilon_0}$$

where $d\sigma$ is the change in plateau stress, T is the test temperature, ΔH is the latent heat of transformation (obtained from DSC measurements) and ε_0 is the transformational strain. To display the superelastic behavior in the working temperature range, it is required to have the finish temperature of austenite transformation, A_f, below the oral cavity temperature. Also, the differential between the A_f and the oral (working) temperature decides the critical stress for stress-induced martensite transformation, which dictates the actuation force; this should reach the required force for the type of teeth that the arch-wire will be actuating on.

Ni–Ti SMAs in wire form are obtained by thermo-mechanical processing routes through a combination of forging, rolling, and cold-drawing to achieve 30–50% reduction in cross-section area followed by intermediate annealing [17]. As a consequence of these adopted thermo-mechanical processes, the signatures of transformation such as start and finish temperatures of transformation [18–20], the occurrence of one step or multistep martensitic transformation, or the enthalpy can be largely tailored together with maintaining close dimensional tolerances during processing [21,22]. These processes can be understood from the microstructure point of view, as all these processes govern the microstructural development which greatly affects the physical properties and mechanical behavior of the Ni–Ti alloys. However, previous studies on microstructure development in these alloys with respect to thermally induced transformation were limited primarily in understanding the formation and distribution of metastable precipitates, dislocation arrangements and local stress fields which alter the mechanics of martensitic transformation. These researches have shown that these factors individually or in combination can delay or suppress the martensitic transformation or induce a two-step transformation [23]. What is understood is that these processes in combination with different heat treatments lead to precipitation of certain metastable phases such as Ni_3Ti_2 and Ni_4Ti_3 [24–27] that establish coherent stress fields with the matrix. These external stresses may favor the appearance of certain martensite variants over others that dictates the phase transformation or induce a second transformation. However, to date, no study exists linking intermediate stages of thermo-mechanical processes for fabrication of orthodontic wires to control the transformation window with direct microstructural observations: changes in grain size and shape, nature of interfaces, in-grain misorientations, residual martensite content, etc. This had been the motivation behind the present study.

The objective of this study was to index the possible microstructural development by direct electron backscattered diffraction (EBSD) and X-ray diffraction measurements to the calorimetric signatures of phase transformation.

2. Experimental methods

Ni–Ti (50.8 at.% Ni and 49.2 at.% Ti) alloy button was prepared by vacuum induction melting (VIM). The cast button was further remelted through the vacuum arc remelting (VAR) process. The secondary melting process (after VIM) was

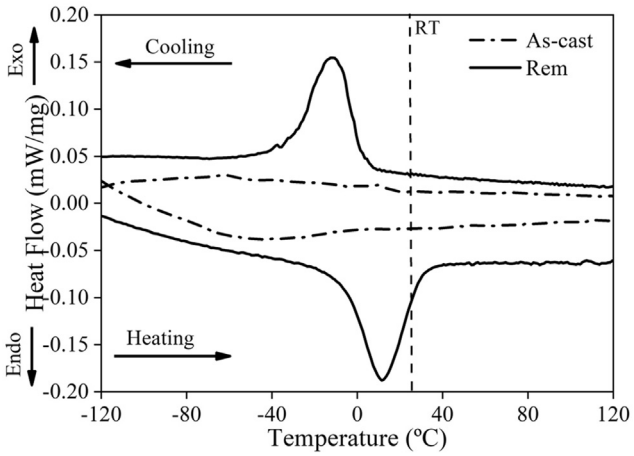

Fig. 1 – DSC results for as-cast and remelted sample. The remelting was sufficient to regain the calorimetric signatures of the phase transformation with a high degree of control over the microstructural homogeneity.

sufficient to bring back calorimetric signatures of austenite ↔ martensite transformations with a high degree of control over the microstructural homogeneity (Fig. 1).

A relatively complex thermo-mechanical schedule was used, summarized in Fig. 2. The adopted thermo-mechanical process involved four hot forgings followed by two subsequent cold forging steps with approximately 10, 20, 14, 17 and 40% reduction in diameter respectively at each step; after each forging step, the samples were subjected to annealing treatment (800 °C/10 min). The 2nd cold forging step reduced the final diameter to 3 mm. As mentioned earlier, the stated objective of the present research was to identify the phase transformation patterns after selected intermediate processing steps and correlate them with the corresponding microstructure. The study was limited to remelted (sample A), the first-hot forged (sample B), and the cold-forged samples (sample C and D) (Fig. 2). For the production of orthodontic archwires, diameters are usually further reduced to desirable sizes through final cold drawing, but the present work deals with studying the transformation characteristics during primary processing stages. So, the final wire drawing process was not included within the scope of the present study.

The samples were subjected to standard metallographic techniques for surface preparation followed by electropolishing using a Struers Lectropol 5 system: 18 V DC, the electrolyte of 80:20 (by volume) methanol: perchloric acid at 273 K (0 °C).

For electron backscattered diffraction (EBSD) analysis, measurements were performed in a FEI Quanta-3D field emission gun-scanning electron microscope (FEG-SEM) with Tex-SEM Laboratories (TSL)-Orientation Imaging Microscopy (OIM™) EBSD system. Typically, the scan step size of 0.5 μm was maintained for all samples under investigation. Data points above 0.1 CI (confidence index) values were taken for all successive analyses. CI (on a scale of 0–1) determines the accuracy of automatic indexing. CI values above 0.1 represent more than 95% success [29]. For EBSD analysis the definition of grains must be clearly understood. Grains were defined as regions continuously bounded by misorientation >5°. Typically, low angle boundaries (LAGB) s had boundary misorientation between (2–5)° while medium angle boundaries (MAGB) s showed (5–15)° misorientation. Misorientation >15° were identified as high angle grain boundary (HAGB) s. Grain average misorientation (GAM) values were taken as the average point-to-point misorientation inside all identified grains. For accurate identification of the martensite phase, a minimum of 5 Hough peaks and optimized indexing parameters were used [30]. This effectively eliminated the chances of incorrect phase identification.

High-energy Synchrotron radiation X-ray diffraction (SR-XRD) data were obtained at beamline (P07) of PETRA III

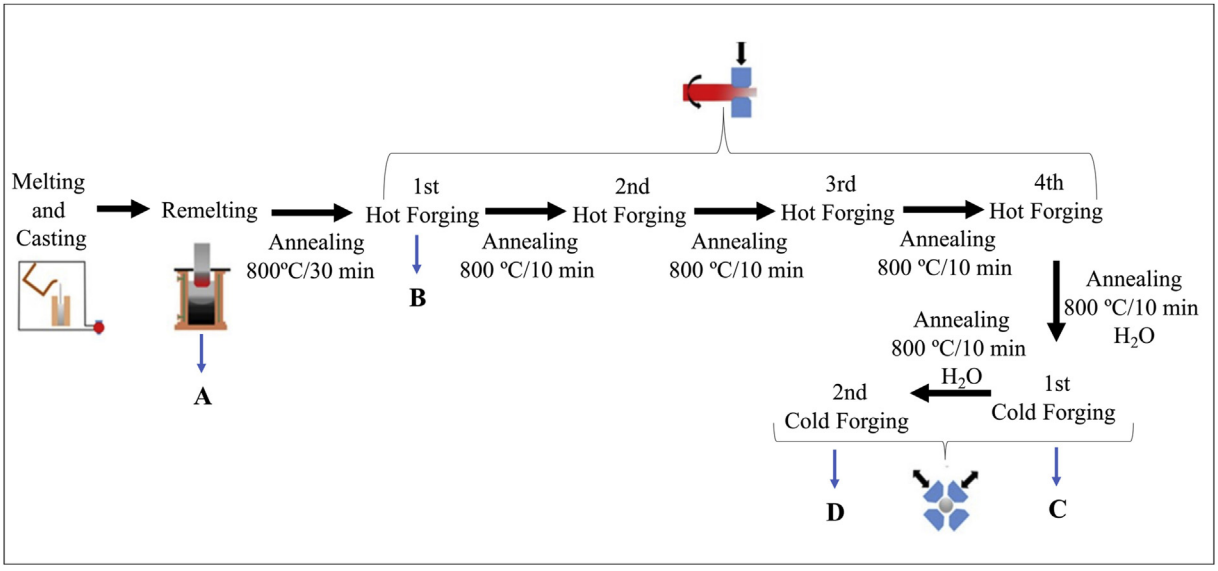

Fig. 2 – Schematic of the adopted thermo-mechanical process. This involved a combination of four hot and two cold forging steps; after each forging step, the samples were subjected to annealing treatment.

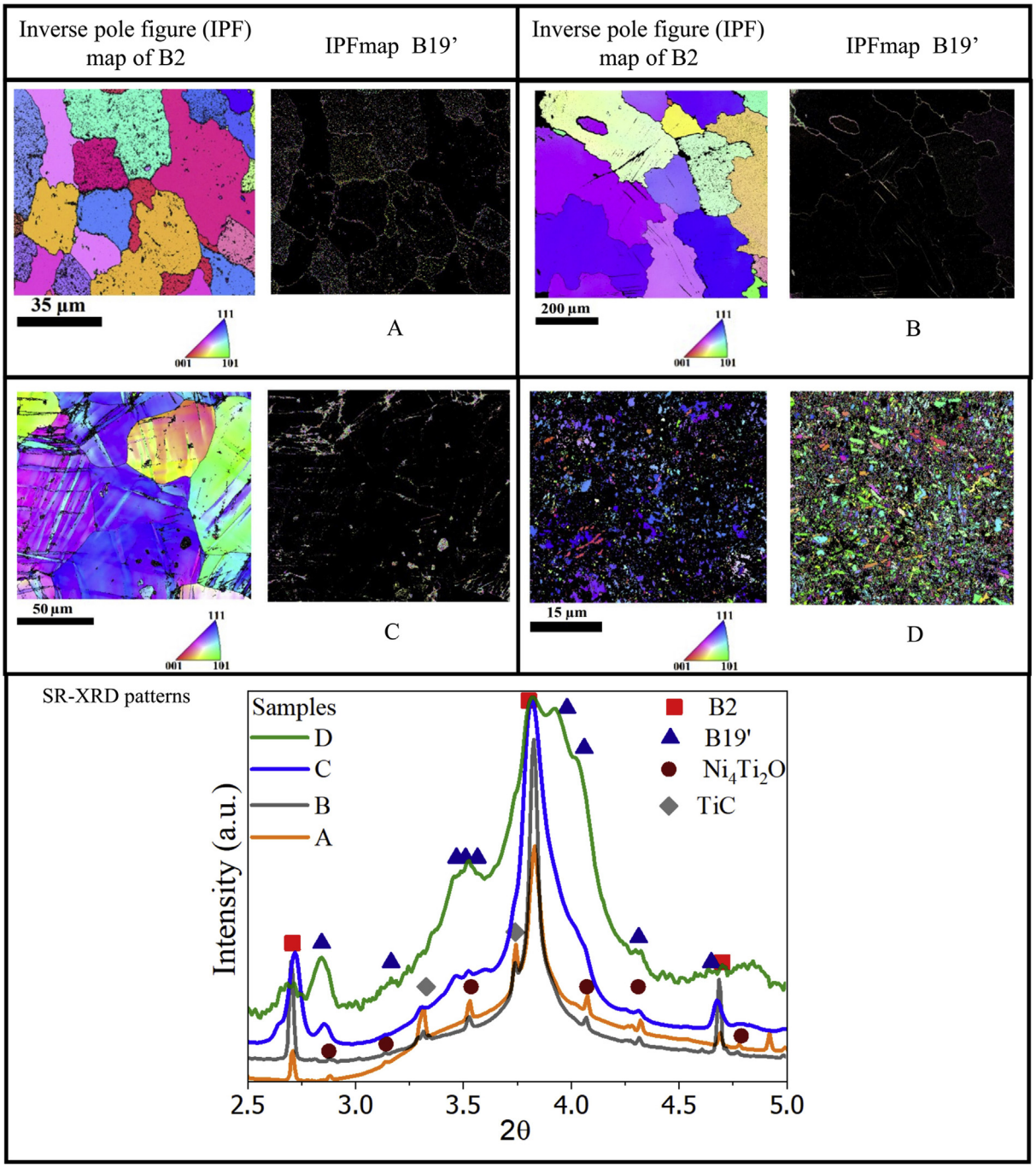

Fig. 3 – Microstructural developments through the adopted thermo-mechanical processes for the remelted (A), first hot forged (B), first cold forged (C) and second cold forged (D) samples. Inverse pole figure (IPF) maps of the austenite and martensite phases are included. Also included is the normalized X-ray diffraction plots showing the identification of the major peaks. Though EBSD measurement within the scan limited area could not bring out significant presence of (110) orientations of the B2 austenite phase, XRD diffraction plot did show strong (110) peak, which is attributed to its higher scattering factor.

synchrotron radiation source at DESY (Hamburg, Germany). The SR-XRD provides a huge collection of diffraction data for the complete determination of the crystallographic structure of materials in minutes [31]. For the high-energy X rays, the sample absorption is relatively small, making it possible to study 1 mm thick samples in transmission geometry. The samples were sectioned perpendicular to the longitudinal direction. A beam of monochromatic X-ray with the energy of 87 keV (wavelength of 0.1425 Å) and a beam spot size of 200 × 200 μm^2 was used-. A two-

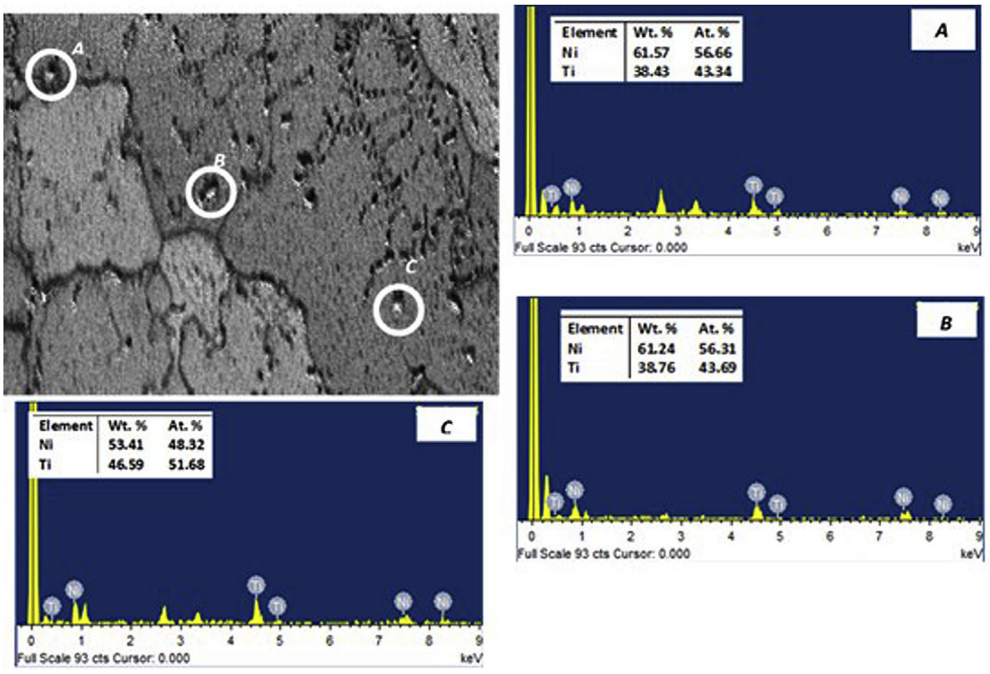

Fig. 4 – Presence of precipitates along grain boundaries and grain interiors. Energy dispersive X-ray measurement for few random precipitates suggests that these precipitates were Ni_4Ti_3 and other complex intermediates.

dimensional digital flat panel X-ray detector (Perkin Elmer XRD 1621) positioned at 1.35 m behind the sample was used to record the diffracted rays. The measured raw data consisted of a series of two-dimensional diffraction patterns which were treated using the Fit2D program to obtain the corresponding one-dimensional diffraction patterns by integration for Phi from 0 to 360° [32]. All peaks were successfully indexed using the ICDD (International Centre for Diffraction Data) database.

For calorimetric measurements, samples were studied using a DSC 204 F1 Phoenix differential scanning calorimetry (DSC) equipped with a LN_2 cooling attachment and an inert gas (N_2) atmosphere. The heating–cooling cycles for all thermo-mechanically processed specimens were performed in the temperature span of −150 to 150 °C at the rate of 10 K min^{-1}.

3. Results and discussion

3.1. *Microstructure development*

Fig. 3 summarizes the evolution of the microstructures during processing as seen in the EBSD-measured IPF (inverse pole figure) maps estimated for both austenite and martensite phases. A better description of the presence of phases is available in the XRD (X-ray diffraction) plots. The colors in the IPF maps refer to the directions (NDs) perpendicular to the EBSD scan plane (cross-sectional plane of the cylindrical samples). The typical microstructures included are refined grains with serrated boundaries (sample A), large grains with

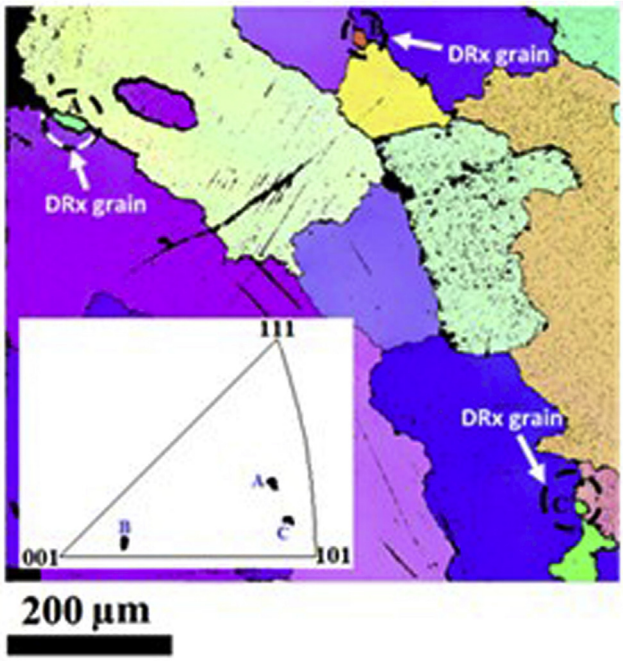

Fig. 5 – Large size grains with serrated grain boundaries is observed for the first hot forged sample B. Often these microstructures were characterized by presence of fine sized grains residing in grain boundaries and triple junctions. The orientation of these fine sized grains (shown in the inset) had larger spread than statically recrystallized grains, suggesting that these grains were dynamically recrystallized.

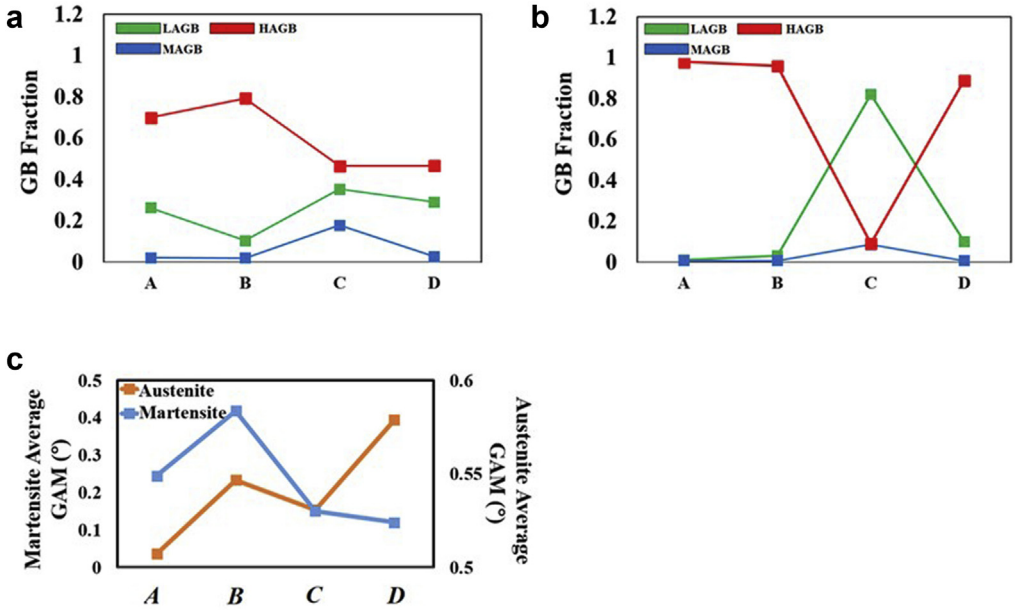

Fig. 6 – Clear differences in grain boundary fractions and local in-grain misorientation between different samples are seen. (a) Austenite B2 and (b) martensite B19′ grain boundary fractions plotted for samples A, B, C and D. (c) Average misorientation (GAM) plotted for all samples.

serrations (sample B), the presence of twin-like bands in the parent austenite grains (sample C), and fine-grained distribution of austenite and martensite phases (sample D). A careful look into the IPF orientation maps of B2 austenite showed the presence of black regions (non-indexed regions) which had data points of CI $\leq$ 0.1. Typically, the B19′ monoclinic martensite structure is often difficult to characterize by XRD and EBSD; it must be pointed out that the presence of martensite was also observed in these "black" regions, under the conditions of detection of a minimum of five diffraction bands and CI > 0.1. It must also be noted that each different microstructure had varying austenite grain sizes, as apparent in the IPF maps, hence it was not possible to maintain identical scan sizes for all specimens.

Sample A presents a homogenized microstructure. The serration in the boundaries seen in sample A was due to possible precipitation of secondary phases that caused pinning during the boundary migration. The image quality (IQ) map in Fig. 4 for a magnified region of sample A shows the distribution of precipitates in the austenite boundaries.

SR-XRD measurements further clarified the presence of oxides (Ni_4Ti_2O) and TiC on samples A and B or possibly overlapping with other peaks for samples C and D. The X-ray measurement for compositional analysis were performed on few randomly distributed precipitates of different size and shapes, indicated by suitable markers. The location of such precipitates was found both in grain interiors and boundaries. The EDS spectra measured for few different precipitates are also included for reference in Fig. 4. The chemical composition suggests that some of these precipitates corresponded to either Ni_4Ti_3 or some other complex intermediates. Unfortunately, these precipitates could not be indexed by EBSD due to their smaller size below the spatial resolution of the EBSD. The SR-XRD did not allow the clear identification of Ni_4Ti_3 also due to their fine dispersion and overlapping with peaks of other phases. It is interesting to note that the remelted sample had a fine presence of martensite, mainly visible in the grain boundaries. Available literature on remnant martensite have shown their presence is largely due to deformation [9] or thermal cycling [33] without intermediate annealing. The observation in the present study indicates that the electropolishing treatment of the sample at sub-zero temperature introduced transformation in the specific region. Reversal of phase transformation led to a small amount of martensite in the microstructure and local misorientation (microstructural strain) seen as non-indexed points.

The SR-XRD data for <110> B2 peaks clearly shows a general trend of gradual broadening from A to D samples. This may be assigned to the microstructural evolution from A (remelted) to B (hot-forged) and, finally C (first cold-forging) and D (second cold-forging) and correspondingly increasing structural defects density along this processing path. Also, along this processing path, it is possible to notice a significant decrease of the intensity of both Ni_4Ti_2O and TiC from samples A to B due to particle cracking during hot deformation. For samples C and D these peaks from Ni_4Ti_2O and TiC are even less evident due to a combination of the continuing deformation cracking of these particles and the increasing amounts of overlapping broad martensite peaks.

Sample B showed the presence of large grains with serrated grain boundaries. During hot forging, the pre-existing grain boundaries elongated along the deformation direction causing grain boundary serration. A closer look into the microstructure represented in Fig. 5 also brings out fine grains

of austenite sparsely distributed along these serrated boundaries. These grains appear to be dynamically recrystallized. The point is validated through the IPF triangle notation in the inset, showing that these fine grains often had a larger orientation spread than typical recrystallized (static) grains.

More importantly, combinations of hot and cold deformation with short annealing treatments induced significant differences in in-grain misorientation and grain boundary fractions for both phases, illustrated in Fig. 6a–c. Since martensite had limited volume (area) fractions, it was therefore necessary to use relatively "limited" EBSD statistics.

The cold forged-annealed microstructure in sample C was characterized by several twin-like features which are signatures of cold deformed microstructure illustrated in Fig. 7a. It appears that the adopted annealing treatment initiated recovery of the microstructure to bring back reversibility of austenite–martensite phase transformation without destroying the cold worked microstructure. This point will be discussed under the transformation behavior in a later section. The twin-like bands were seen to be the only source of HAGBs inside the parent austenite grains. These bands were seen to run as parallel needles that mainly go through the parent austenite grains and stop at grain boundaries. Although these bands comprised both medium and high angle boundaries as shown in the IQ plus grain boundary map in Fig. 7a, some of these had a (54–56)° <110> orientation relationship (OR) with the parent austenite grains. The IQ map in Fig. 7b showed poor contrast around the bands (darker bands) suggesting that these bands accommodated larger strains in the grain interior. One or two sets of intersecting parallel needles can be seen within the parent austenite grains. The presence of residual martensite was mostly visible around the HAGBs of a single twin-like feature or at the intersection of two bands, as indicated by the arrow marks in Fig. 7c. The cold forging induced certain martensite variants which were favorably oriented to the straining axis to grow; however,

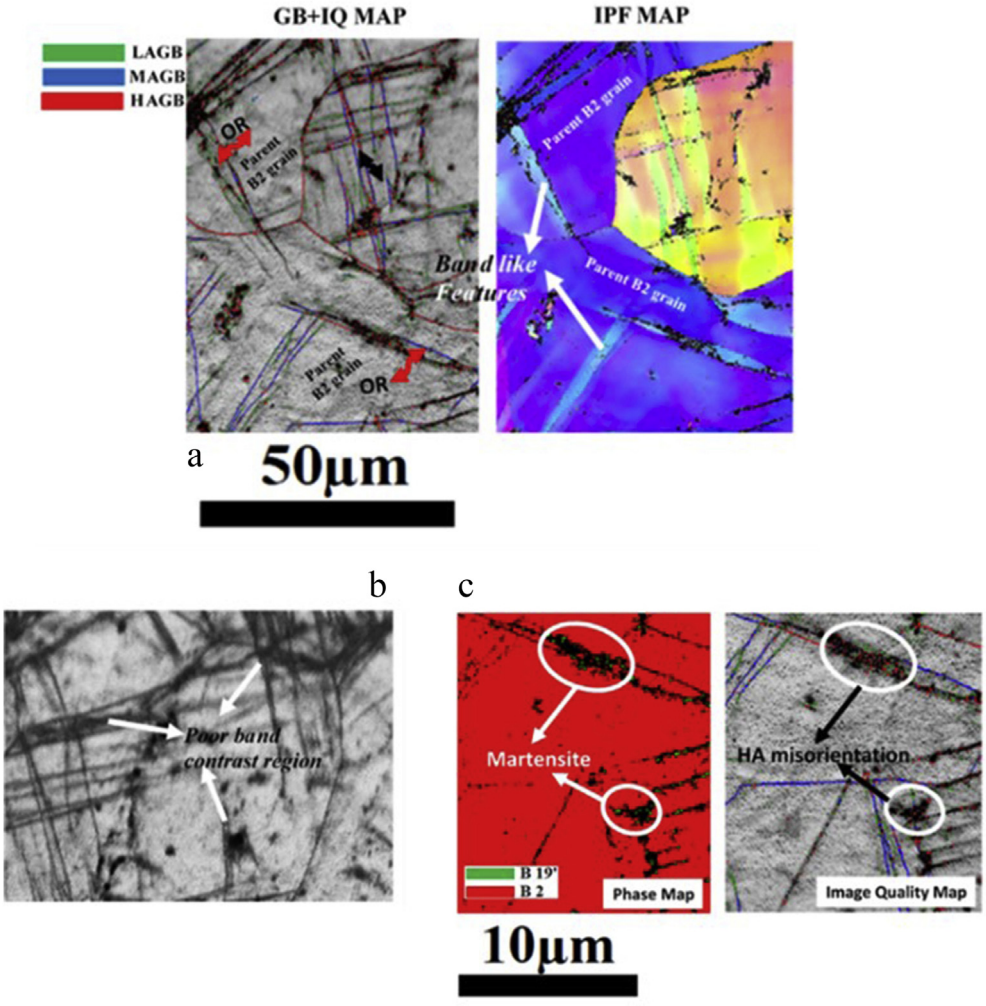

Fig. 7 – Microstructure of the cold forged sample C. (a) Twin-like bands within parent austenite grains seen through grain boundary plus band contrast and orientation image maps. These bands had a (54–56)° <110> orientation relationship (OR) with the surrounding austenite grains. (b) Band contrast map showing poor band contrast around the twin-like features seen as dark regions implying large strain accumulation in the bands. (c) Visible retained martensite seen within the twin-like bands represented through phase and band contrast map. The retained martensite presence was largely seen in the high angle misorientation boundaries.

beyond a certain stress value, the deformation of the martensite took place under irreversible slip mode. This led to the creation of certain new variants that could not transform back to austenite during the reversion process. Thus, the retained martensite is attributed to the local strain inhomogeneities, initial microstructure and the applied stresses.

The regions of a high density of twin-like bands provided the growth of martensite at the later stages of cold forging. This point is illustrated in Fig. 8 showing large factions of visible martensite evenly distributed in the parent austenite. This could be due to the stabilization of the B19′ martensite by the pinning of the interface by the defects introduced. The OR measured between the parent-product phases attempted manually for approximately 20 B2–B19′ interfaces were found to be close to the ORs previously determined between the twin-like features and the austenite matrix. One may therefore speculate this twin-like features as transforming bands. For a given OR, there remains an axis that is invariant relative to the transformation. In such a situation, the product lattice may be described by a rotation angle θ about an axis of rotation <*uvw*>. Depending on the specific OR assumed between the parent and product lattices, a parent B2 orientation may be transformed into several corresponding B19′ variants. As stated earlier in this section, any cold forming process introduces plastic deformation in the martensite variants causing the formation of new variants through a reorientation

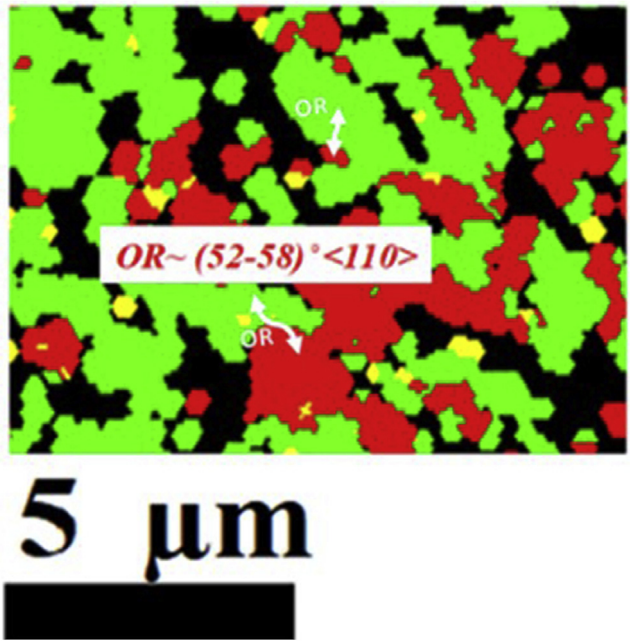

Fig. 8 – Phase map of a selected region of sample D showing martensite (green) and austenite (red) phases. The OR measured for randomly 20 B2–B19′ interfaces was found to range between (52–58)° <110>. The observed OR matches well with the OR established between the twin-like features and parent austenite grains in sample C. It suggests that the martensite in sample D resulted from the transformation of twin like features during the cold forging step.

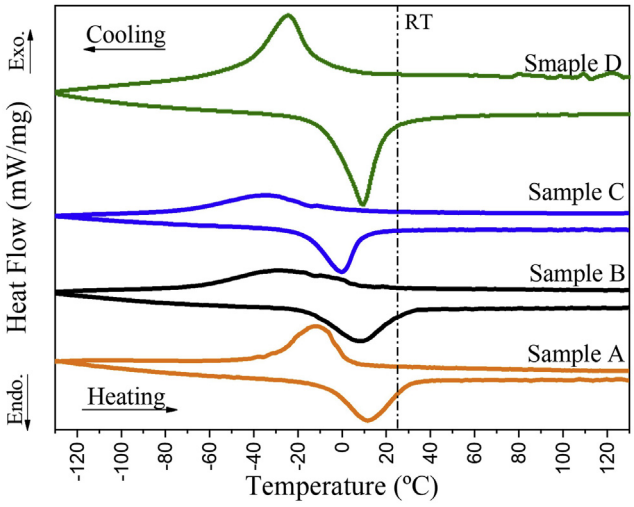

Fig. 9 – Differential scanning calorimetry (DSC) thermograms during (a) cooling and (b) heating for samples A, B, C and D.

process. However, the interfaces of some of these variants retain the OR with the parent phase but do not transform due to a large accumulation of defects. The higher GAM value measured for martensite is consistent with an accumulation of defects in the structure.

The normalized X-ray spectra corresponding to the principal peaks of austenite and martensite are shown in Fig. 3. The peaks refer to reflections from the lattice planes containing the cylindrical–longitudinal axis. The most isolated martensite peaks could be indexed, while other peaks have been suppressed due to "broadening effects" resulting from partial overlap. The visible changes in the ⟨100⟩ and ⟨111⟩ peak intensities imply a change in the austenite texture with progressive deformation and treatment. However, with "limited" statistics on grain orientations within the scan area of EBSD, texture (microtexture) measurements were not possible to be studied in the present research. Some discrepancy was found between the visible austenite orientations measured by EBSD versus corresponding indexed austenite peaks in XRD. The strong appearance of (110) peak of B2 in all samples is likely due to its higher structure factor. Also, scattering factors for similar diffracting planes change significantly while moving from X-rays to electron diffraction leading to differences in intensities. The IPF map of sample D shows a strong presence of ND//⟨111⟩ which is not reflected in the corresponding peak

Table 1 – Phase transformation temperature and enthalpy for A, B, C and D samples.

	Cooling			Heating (°C)			
	M_s (°C)	M_p (°C)	M_f (°C)	A_s (°C)	A_p (°C)	A_f (°C)	ΔH (J/g)
A	0.7	−10.8	−28.0	−6.4	11.6	30.1	17
B	7.2	−29.4	−59.0	−15.1	9.2	27.5	18
C	−16.8	−35.1	−87.6	−16.5	−0.2	8.7	15
D	−15.6	−2.6	−36.2	1.7	13.4	20.2	21

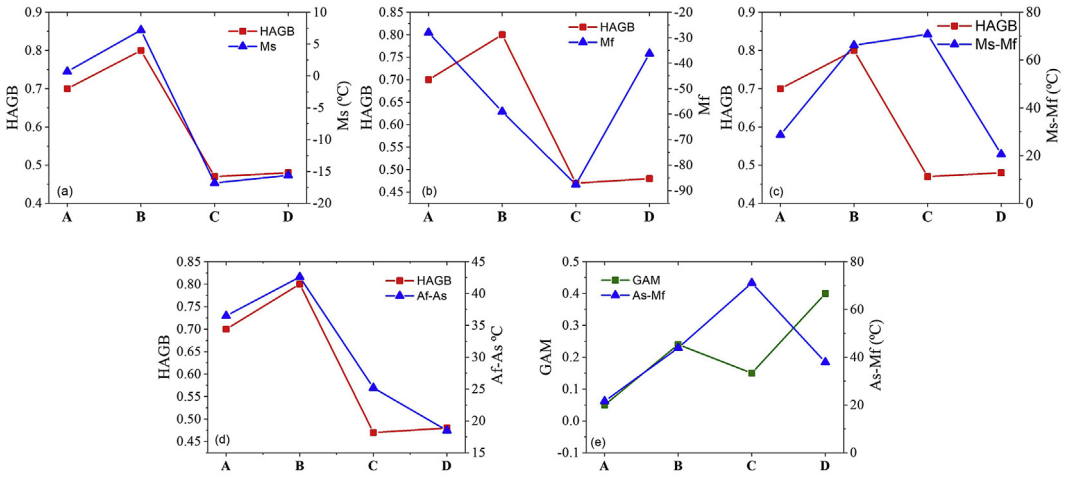

Fig. 10 – (a) Martensite start (M_s) and (b) Martensite finish (M_f) temperatures estimated from DSC measurements plotted with high angle boundary (HAGB) fraction for samples A, B, C and D. M_s correlated directly with HAGB, while M_f exhibited an inverse trend. (c) M_s–M_f and (d) A_f–A_s transformation intervals also showed direct correlation with HAGB fraction. (e) The reverse transformation hysteresis, A_s–M_f and GAM exhibited nearly similar trend.

position in the diffractogram, roughly at 4.7°. This result is due to peak broadening related to the contributions from B19′.

3.2. *Phase transformation characteristics*

The DSC measurements in terms of transformation enthalpy and transformation temperature are included in Table 1 for reference. The results on transformation characteristics for samples A, B, C and D are illustrated in the DSC plots in Fig. 9.

It was observed in the present study that M_s scaled identically with HAGB fraction as shown in Fig. 10a. The M_s temperature decreased with the cold forging steps. A decrease in the M_s temperature implies difficulties in direct transformation. Cold forging introduced significant dislocation density seen through increased GAM (Fig. 6c). Annealing at 800 °C did not eliminate dislocations but led to the recovery of microstructures. These dislocations formed substructures within the grains at the expense of the HAGB. Therefore, a decrease in the HAGB fraction was observed with a concurrent increase in GAM. There exist several theories for martensite nucleation and propagation. The most accepted phenomenological theory says that transformation of austenite to martensite phase proceeds with the formation of glissile dislocation interfaces [34] i.e. periodic arrangement of dislocations in order to minimize the elastic strain energy associated with the phase interface [35]. The growth of the martensitic transformed region is determined by the dislocation motion and proceeds as long as the transformation interface maintains the glissile nature. During the thermal initiation of martensite in polycrystalline grains, the crystallographic variants of the martensite phases form plate-like morphologies that grow within an austenite grain to minimize elastic strain energy associated with shape and volume change. However, the growth is hindered when encountering a strong barrier, typically high grain boundary, entangled dislocations (or dislocation substructures), or a previously formed martensite plate [36]. The fine-grained austenite microstructure also offers greater hindrance and acts as a barrier to the growth of martensite plates. In the present study, the grain size was reduced in successive operations. It has also been observed in this investigation that the density of precipitates inside the grain was lower for all samples, so the internal stress caused by the precipitation of secondary phases is lower inside the grain than near the boundaries. It is thus the internal stress that suppresses the martensitic transformation, which decreases with increasing grain size. Although the suppression in the M_s temperature was due to the combined effect of reduced grain size, internal stresses caused by the precipitates and dislocation substructures, the present investigation was consistent with a fraction of HAGBs. Conversely, the M_f temperature showed a different trend with the HAGB fraction, see Fig. 10b. More importantly, from a thermodynamic point of view, the transformation temperature ranges (M_s–M_f and A_f–A_s) have a strong dependence on the friction energy against the migration of the habit plane and the elastic energy stored by the growth of the martensite plates. The friction energy opposing the driving force of the martensite propagation is correlated with the stored energy of the austenite grains. It is reported that the stored energy of the austenite grains is a function of the HAGB fraction and the dislocation distribution. The present results in Fig. 10c suggest that decreasing HAGBs, increases the mobility of the habit plane, thereby reducing the friction energy to oppose the transformation. This is consistent with the lowering of M_s–M_f in the last deformation stage. On the other hand, the increased dislocations density due to cold forging in the B2 phase may have relaxed the stored elastic strain energy of martensite plates and resulted in the narrowing of reverse transformation A_f–A_s peak from hot deformations to cold deformation stages, see Fig. 10d.

The transformation hysteresis can be ascribed to the dislocations introduced during stages of processing. Although A_f–M_s did not show any correlation with microstructural parameters, A_s–M_f clearly showed a good correlation with the

GAM as shown in Fig. 10e. The reverse transformation hysteresis corresponds to the energy that is dissipated to overcome frictional energy work that opposes interfacial movement during transformation [37,38]. The role of the dislocation that constitutes the martensite–austenite interface is to reduce the internal stress of the martensite variants at the habit plane, thus relaxing the strains at the interface. Increase in the dislocation density seen through increased GAM imposes larger frictional resistance to the habit plane motion during reverse transformation. This relates to the decrease in the A_s–M_f hysteresis (Fig. 10e) and increasing enthalpy of the reverse transformation (Table 1) with progressive cold deformation.

The applied thermomechanical process applied may allow to produce a material with a superelastic behavior close to the oral temperature, which is relevant in dentistry applications, namely for orthodontic archwires. The A_f temperature is the most important temperature to determine from the clinical and manufacturers point of view, because at this temperature the alloy is stable and exhibits the final adequate shape for the application that is aimed [39]. Moreover, the microstructure that is present at room temperature is fundamental to define their application as a superelastic device.

4. Conclusions

(1) Significantly different microstructures were produced during each stage of the processing. The microstructures had large grain size which is characteristic of cast microstructures, grain boundary serrations, twin-like bands within austenite grains and mixed-phase distribution of austenite and martensite. All these microstructures had direct or indirect effect on the transformation behavior of the alloy.

(2) The twin-like bands of austenite obeyed a specific orientation relationship (OR) with the surrounding austenite matrix in the first cold-forged sample. The observed OR was (54–56)° <110>. These bands were identified as transforming bands. An identical OR was observed between the martensite and austenite in the second cold-forged sample. It was therefore concluded that these bands were the first to transform to martensite in the next cold forging step.

(3) The martensite start and finish temperatures (M_s, M_f) were well correlated with high angle grain boundary (HAGB) fractions. While M_s directly related to HAGB fractions, M_f showed a different trend. The HAGB fraction is also related to the transformation intervals. The hysteresis for the reverse transformation of martensite to austenite correlates well with the in-grain misorientation.

(4) The overall role of the successive hot and cold forging steps is put in evidence by the decreasing intensity of the XRD peaks of Ni_4Ti_2O and TiC (due to decreasing particle sizes) and the increasing relevance of the martensite peaks along the processing route.

Declaration of Competing Interest

The authors declare that they have no known competing financial interests or personal relationships that could have appeared to influence the work reported in this paper.

Acknowledgments

This work was financially supported by: Project PTDC/CTM-CTM/29101/2017 – POCI-01-0145-FEDER-029101 funded by FEDER funds through COMPETE2020 – Programa Operacional Competitividade e Internacionalização (POCI) and by national funds (PIDDAC) through FCT/MCTES. This research was also supported by FEDER funds through the program COMPETE – Programa Operacional Factores de Competitividade, and by national funds through FCT – Fundação para a Ciência e a Tecnologia, under the project UIDB/EMS/00285/2020. F.M.B.F. acknowledges the funding of CENIMAT/I3N by National Funds through the FCT - Fundação para a Ciência e a Tecnologia, I.P., within the scope of the project ref[a] UIDB/50025/2020-2023. A.S.P, and P.F.R. acknowledge the funding of CAPES (APQ-1 2009/02 E-26/110.414/2010, APQ-1 2011-2 E-26/110.269.2012, E-26/111.435/2012 – CsF/Brazil – BEX 11943-13-0) and CNPq (research productivity scholarship PQ-2 – Process 307798/2015-1).

REFERENCES

[1] Costanza G, Tata ME. Shape memory alloys for aerospace, recent developments, and new applications: a short review. Materials (Basel) 2020;13:1856. https://doi.org/10.3390/MA13081856.

[2] M S, Sheikh MY, Khan N, Kurbet R, Gowda TMD. A review on application of shape memory alloys. Int J Recent Technol Eng 2021;9:111–20. https://doi.org/10.35940/ijrte.F5438.039621.

[3] Zhou D, Gao Y, et al. A review of shape memory alloy research, applications and opportunities. Mater Sci Eng A 2015;56:1078–113. https://doi.org/10.1016/j.matdes.2013.11.084.

[4] Rodrigues PF, Fernandes FMB, Magalhães R, Camacho E, Lopes A, Paula AS, et al. Thermo-mechanical characterization of NiTi orthodontic archwires with graded actuating forces. J Mech Behav Biomed Mater 2020;107:103747. https://doi.org/10.1016/j.jmbbm.2020.103747.

[5] Kotha RS, Alla RK, Shammas M, Ravi RK. An overview of orthodontic wires. Trends Biomater Artif Organs 2014;28:32–6.

[6] Naresh C, Bose PSC, Rao CSP. Shape memory alloys: a state of art review. In: IOP Conf Ser Mater Sci Eng, vol. 149. Institute of Physics Publishing; 2016. https://doi.org/10.1088/1757-899X/149/1/012054.

[7] Cho H, Yamamato T, Takeda Y, Suzuki A, Sakuma T. Exploitation of shape memory alloy actuator using resistance feedback control and its development. Prog Nat Sci Mater Int 2010;20:97–103. https://doi.org/10.1016/s1002-0071(12)60013-6.

[8] Mirvakili SM, Hunter IW. Fast torsional artificial muscles from NiTi twisted yarns. ACS Appl Mater Interfaces 2017;9:16321–6. https://doi.org/10.1021/acsami.7b02335.
[9] Basu R, Szpunar J, Eskandari M, Mohtadi-Bonab MA. Microstructural investigation on marforming and conventional cold deformation in Ni-Ti-Fe based shape memory alloys. Int J Mater Res 2015;106:852–62. https://doi.org/10.3139/146.111252.
[10] Dos Santos Paula A, Canejo JPHG, Silva RJC, Fernandes FMB. Effect of thermal cycling on the transformation temperatures of a Ni-Ti shape memory alloy. Mater Sci Forum 2004;455–456:346–50. https://doi.org/10.4028/www.scientific.net/msf.455-456.346. Trans Tech Publications Ltd.
[11] Silva JD, Resende PD, Garcia PR, Azevedo Lopes NI, Arruda Santos L, Buono VTL. Fatigue resistance of dual-phase NiTi wires at different maximum strain amplitudes. Int J Fatigue 2019;125:97–100. https://doi.org/10.1016/j.ijfatigue.2019.03.040.
[12] Yoneyama T, Miyazaki S, Luo H, Liao Y, Abel E, Wang Z, et al. Shape memory alloys for biomedical applications. https://doi.org/10.1016/S1369-7021(08)70257-8; 2010.
[13] Fischer H, Vogel B, Pfleging W, Besser H. Flexible distal tip made of nitinol (NiTi) for a steerable endoscopic camera system. Mater Sci Eng A 1999;273–275:780–3. https://doi.org/10.1016/s0921-5093(99)00415-3.
[14] Kim SW, Park CH, Kim JH, Hong JK, Yeom JT. Effect of plastic working on martensitic phase transformation characteristics of TiNi alloys. J Alloy Compd 2014;610:315–21. https://doi.org/10.1016/j.jallcom.2014.04.205.
[15] Malik Nidhi, Dubey Rachna, Kallury Amitabh, Chauksye Ankur, Shrivastav Trilok, Kapse Bhagwat Rao. A review of orthodontic archwires. J Orofac Res 2015;5:6–11.
[16] Suzuki Y, Horikawa H. Thermal hysteresis in Ni-Ti and Ni-Ti-X alloys and their applications. MRS Proc 1991;246. https://doi.org/10.1557/proc-246-389.
[17] Pelton AR, Dicello J, Miyazaki S. Optimisation of processing and properties of medical grade Nitinol wire. Minim Invasive Ther Allied Technol 2000;9:107–18. https://doi.org/10.3109/13645700009063057.
[18] Yeom J-T, Kim JH, Hong J-K, Kim SW, Park C-H, Nam TH, et al. Hot forging design of as-cast NiTi shape memory alloy. Mater Res Bull 2014;58:234–8. https://doi.org/10.1016/j.materresbull.2014.04.049.
[19] Lekston Z, Zubko M, Lelątko J, Stróż D, Goryczka T, Wierzchoń T, et al. The structure and properties formation of the NiTi shape memory rods after hot rotary forging. Key Eng Mater 2016;687:11–8. https://doi.org/10.4028/www.scientific.net/KEM.687.11.
[20] Shahmir H, Nili-Ahmadabadi M, Naghdi F. Superelastic behavior of aged and thermomechanical treated NiTi alloy at $A_f + 10\,^{\circ}C$. Mater Des 2011;32:365–70. https://doi.org/10.1016/j.matdes.2010.06.022.
[21] Chrobak D, Stróż D. Two-stage R phase transformation in a cold-rolled and annealed Ti-50.6 at.% Ni alloy. Scr Mater 2005;52:757–60. https://doi.org/10.1016/j.scriptamat.2004.12.010.
[22] Dehghani K, Khamei AA. Hot deformation behavior of 60Nitinol ($Ni_{60wt\%}$–$Ti_{40wt\%}$) alloy: experimental and computational studies. Mater Sci Eng A 2010;527:684–90. https://doi.org/10.1016/j.msea.2009.08.059.
[23] Prokoshkin S, Brailovski V, Inaekyan K, Korotitskiy A, Kreitcberg A. Thermomechanical treatment of TiNi intermetallic-based shape memory alloys. Mater Sci Found 2015;81–82:260–341. https://doi.org/10.4028/www.scientific.net/msfo.81-82.260.
[24] Chiang LJ, Li CH, Hsu YF, Wang WH. Age-induced four-stage transformation in Ni-rich NiTi shape memory alloys. J Alloy Compd 2008;458:231–7. https://doi.org/10.1016/j.jallcom.2007.04.006.
[25] Kabayama LK, Rigo OD, Otubo J. Influence of thermomechanical processing on the martensitic transformation temperatures of NiTi SMA wire. Mater Sci Forum 2010;643:43–8. https://doi.org/10.4028/www.scientific.net/MSF.643.43. Trans Tech Publications Ltd.
[26] Schmahl WW, Khalil-Allafi J, Hasse B, Wagner M, Heckmann A, Somsen C. Investigation of the phase evolution in a super-elastic NiTi shape memory alloy (50.7 at.% Ni) under extensional load with synchrotron radiation. Mater Sci Eng A 2004;378:81–5. https://doi.org/10.1016/j.msea.2003.11.081.
[27] Qin Q, Peng H, Fan Q, Zhang L, Wen Y. Effect of second phase precipitation on martensitic transformation and hardness in highly Ni-rich NiTi alloys. J Alloy Compd 2018;739:873–81. https://doi.org/10.1016/j.jallcom.2017.12.128.
[29] Schwartz AJ, Kumar M, Adams BL, Field DP. Electron backscatter diffraction in materials science. Springer US; 2009. https://doi.org/10.1007/978-0-387-88136-2.
[30] Nowell MM, Wright SI. Orientation effects on indexing of electron backscatter diffraction patterns. Ultramicroscopy 2005;103:41–58. https://doi.org/10.1016/j.ultramic.2004.11.012. North-Holland.
[31] Gustafson J, Shipilin M, Zhang C, Stierle A, Hejral U, Ruett U, et al. High-energy surface x-ray diffraction for fast surface structure determination. Science 2014;343:758–61. https://doi.org/10.1126/science.1246834 (80-).
[32] Hammersley AP, Svensson SO, Hanfland M, Fitch AN, Hausermann D. Two-dimensional detector software: from real detector to idealised image or two-theta scan. High Press Res 1996;14:235–48. https://doi.org/10.1080/08957959608201408.
[33] Basu R, Jain L, Maji BC, Krishnan M, Mani Krishna KV, Samajdar I, et al. Origin of microstructural irreversibility in Ni-Ti based shape memory alloys during thermal cycling. Metall Mater Trans A Phys Metall Mater Sci 2012;43:1277–87. https://doi.org/10.1007/s11661-011-0970-y.
[34] McCormick PG, Liu Y. Thermodynamic analysis of the martensitic transformation in NiTi-II. Effect of transformation cycling. Acta Metall Mater 1994;42:2407–13. https://doi.org/10.1016/0956-7151(94)90319-0.
[35] Porter DA, Easterling KE, Easterling KE. Phase transformations in metals and alloys [revised reprint]. CRC Press; 2009. https://doi.org/10.1201/9781439883570.
[36] Haldar A, Suwas SBD. Microstructure and texture in steels. Springer London; 2009. https://doi.org/10.1007/978-1-84882-454-6.
[37] Liu Y. Thermodynamic analysis of thermoelastic martensitic transformations. Mater Sci Forum 2004;449–452:1325–8. https://doi.org/10.4028/www.scientific.net/msf.449-452.1325. Trans Tech Publications Ltd.
[38] Hamilton RF, Sehitoglu H, Chumlyakov Y, Maier HJ. Stress dependence of the hysteresis in single crystal NiTi alloys. Acta Mater 2004;52:3383–402. https://doi.org/10.1016/j.actamat.2004.03.038.
[39] Ohara A. Clinical importance of austenitic final point un the selection of nickel-titanium alloys for application in orthodontic-use arches. Rev Odontol Mex 2016;20:162–9. https://doi.org/10.1016/j.rodmex.2016.08.012.